Solar Phys (2018) 293:106
https://doi.org/10.1007/s11207-018-1324-3

Determination of the Coronal and Interplanetary Magnetic Field Strength and Radial Profiles from Large-Scale Photospheric Magnetic Fields

Irina A. Bilenko[1]

Received: 11 March 2018 / Accepted: 4 July 2018 / Published online: 20 July 2018

Abstract We propose a new model for the magnetic field at different distances from the Sun during different phases of the solar cycle. The model depends on the observed large-scale non-polar ($\pm 55°$) photospheric magnetic field and on the magnetic field measured at polar regions from 55° N to 90° N and from 55° S to 90° S, which are the visible manifestations of cyclic changes in the toroidal and poloidal components of the global magnetic field of the Sun. The modeled magnetic field is determined as the superposition of the non-polar and polar photospheric magnetic field and considers cycle variations. The agreement between the model predictions and magnetic fields derived from direct *in situ* measurements at different distances from the Sun, obtained with different methods and at different solar activity phases, is quite satisfactory. From a comparison of the magnetic fields as observed and calculated from the model at 1 AU, we conclude that the model magnetic field variations adequately explain the main features of the interplanetary magnetic field (IMF) radial, B_x, component cycle evolution at Earth's orbit. The modeled magnetic field averaged over a Carrington rotation (CR) correlates with the IMF B_x component also averaged over a CR at Earth's orbit with a coefficient of 0.691, while for seven CR-averaged data, the correlation reaches 0.81. The radial profiles of the modeled magnetic field are compared with those of already existing models. In contrast to existing models, ours provides realistic magnetic-field radial distributions over a wide range of heliospheric distances at different cycle phases, taking into account the cycle variations of the solar toroidal and poloidal magnetic fields. The model is a good approximation of the cycle behavior of the magnetic field in the heliosphere. In addition, the decrease in the non-polar and polar photospheric magnetic fields is shown. Furthermore, the magnetic field during solar cycle maxima and minima decreased from Cycle 21 to Cycle 24. This implies that both the toroidal and poloidal components, and therefore the solar global magnetic field, decreased from Cycle 21 to Cycle 24.

Keywords Magnetic fields, corona · Magnetic fields, interplanetary · Magnetic fields, models · Solar cycle

✉ I.A. Bilenko
bilenko@sai.msu.ru

[1] Moscow M.V. Lomonosov State University, Sternberg Astronomical Institute, Universitetsky pr. 13, Moscow, 119234, Russia

1. Introduction

Solar magnetic fields are swept into interplanetary space by solar wind flows. Solar fields dominate the structure and dynamics of the heliosphere. The heliosphere varies spatially and temporally, following the magnetic field variation. The regularity in magnetic field space and time distribution at different distances from the Sun and during different solar cycle phases are not well known. This is largely due to the weakness of coronal magnetic fields, especially at distances greater than 5 R_s (solar radii). To analyze different processes in the solar corona and interplanetary space, the magnetic field distribution and cycle evolution must therefore be ascertained.

Currently, several different methods are used to measure the coronal magnetic field at different distances from the Sun (Akhmedov *et al.*, 1982; Lin, Penn, and Tomczyk, 2000, Lin, Kuhn, and Coulter, 2004, Bogod and Yasnov, 2016; Gelfreikh, Peterova, and Riabov, 1987). Some measurements of coronal magnetic fields were made at different wavelengths (Lin, Penn, and Tomczyk, 2000; Lin, Kuhn, and Coulter, 2004; Raouafi *et al.*, 2016). The Faraday rotation measurement technique is commonly used to estimate the coronal magnetic field strength within 10 R_s (Pätzold *et al.*, 1987; Sakurai and Spangler, 1994; Spangler, 2005; Ingleby, Spangler, and Whiting, 2007). Pätzold *et al.* (1987) found that the coronal magnetic field at 5 R_s is around 100 ± 50 mG, Sakurai and Spangler (1994) derived magnetic field values at 9 R_s of 12.5 ± 2.3 mG, and Spangler (2005) found a value of 39 mG at 6.2 R_s. Ingleby, Spangler, and Whiting (2007) measured the Faraday rotation with the *Very Large Array* (VLA) at frequencies of 1465 and 1665 MHz and found that the coronal magnetic field is in the range of 46 – 120 mG at a heliocentric distance of 5 R_s. Xiong *et al.* (2013) used coordinated observations in polarized white light and Faraday rotation measurements to determine the spatial position and magnetic field of an interplanetary sheath. Magnetic field values can also be derived from measurements of the solar wind plasma using pulsars (Ord, Johnston, and Sarkissian, 2007; You *et al.*, 2012).

Several methods of magnetic field determination were developed using solar radio emission. Using data from *UltraViolet Coronagraph Spectrometer* (UVCS) *Solar and Heliospheric Observatory* (SOHO) and radio spectrograph observations, Mancuso *et al.* (2003) estimated magnetic field and plasma properties in the active region corona. The results show that the magnetic field is expressed by $B(r) \leq (0.6 \pm 0.3)(r-1)^{-1.2}$ G, which is valid in the range $1.5 \leq r \leq 2.3$ R_s (Mancuso *et al.*, 2003). The magnetic field strength can be derived from the band splittings in type II radio bursts if the coronal density distribution is given (Vršnak *et al.*, 2002; Cho *et al.*, 2007; Hariharan *et al.*, 2014). Using band splitting of coronal type II radio bursts, Cho *et al.* (2007) obtained a coronal magnetic field strength of 1.3 – 0.4 G in the height range of 1.5 – 2 R_s.

Recent investigations demonstrate that shock waves propagating into the corona and interplanetary space, associated with major solar eruptions, can be used to derive the strength of magnetic fields over a very long interval of heliocentric distances and latitudes. The so-called 'standoff-distance' method was developed and is often used now (Gopalswamy and Yashiro, 2011; Gopalswamy *et al.*, 2012; Kim *et al.*, 2012; Bemporad *et al.*, 2016; Schmidt *et al.*, 2016). In this method, a coronal mass ejection (CME) and CME-driving shock dynamics are analyzed. The shock standoff distance, speed, and the radius of the CME flux rope curvature are measured. Alfvén speed and Mach number can be derived using the measured data. Then the magnetic field can be derived by applying a coronal density model. Using this method, Gopalswamy and Yashiro (2011) have found that the magnetic field declines from 48 to 8 mG in the distance range from 6 to 23 R_s. Following the standoff-distance method and using data from the *Coronagraph 2* and *Heliospheric Imager I* instruments on board the

Solar Terrestrial Relations Observatory (STEREO), Gopalswamy *et al.* (2012) have found that the radial magnetic field strength decreases from 28 mG at 6 R_s to 0.17 mG at 120 R_s. They also noted that the radial profile of the magnetic field strength can be described by a power law. Kim *et al.* (2012) performed a statistical study by applying this method to ten fast (≥ 1000 km s^{-1}) limb CMEs (*Large Angle Spectroscopic Coronagraph* (LASCO) *data*) to measure the magnetic field strength in the solar corona in the height range 3 – 15 R_s. They found that the magnetic field strength is in the range 6 – 105 mG. They showed that the magnetic field values derived with the standoff-distance method are consistent with other estimates in a similar distance range.

Despite the increasing number of space missions and the progress made recently in the solar and interplanetary space observations, reliable measurements of the coronal and interplanetary magnetic field (IMF) strength and orientation at different distances and cycle phases do not exist, however. At present, magnetic fields are routinely measured at the photospheric level, besides the National Solar Observatory (NSO) *Synoptic Optical Long-term Investigations of the Sun* (SOLIS)/*Vector Spectromagnetograph* (VSM) also observes the full-disk chromospheric field using the Ca II 8542 nm line, but not in the solar corona and IMF. The magnetic field in the solar corona and interplanetary space is therefore estimated from the observed photospheric fields using different extrapolation techniques into the solar corona. Coronal magnetic fields are investigated and modeled at different distances from the Sun up to several solar radii. Some models at coronal heights are based on the magnetic fields in active regions (Brosius and White, 2006; Bogod and Yasnov, 2008, Bogod, Stupishin, and Yasnov, 2012, Kaltman *et al.*, 2012). Different models are developed both analytically (Banaszkiewicz, Axford, and McKenzie, 1998) and numerically, including magnetohydrodynamics (MHD), magnetohydrostatic, force-free, or potential-field models (Gibson and Bagenal, 1995; Wiegelmann, 2004; Wiegelmann, Petrie, and Riley, 2017, and references therein).

It should also be noted that most models only describe the magnetic field distribution in the radial direction from the Sun. As a rule, in such models the measurements of the magnetic field obtained at different times are summarized in one curve, regardless of a cycle or a cycle phase. However, it is well known that the magnetic field in the quiet corona during sunspot minimum is much lower than the field determined for an average sunspot maximum, and spherical symmetry is not observed. Furthermore, at solar maximum, the magnetic field is different in different solar cycles as a result of different levels of activity. Below the height of ≈ 3 R_s, the magnetic field is governed by the active-region fields. Above a height of ≈ 3 R_s, the radial field, decreasing as R^{-2}, becomes dominant. It should be noted that all coronal magnetic field models that describe magnetic fields above ≈ 3 R_s give only one value for the distance required, regardless the cycle phase. It is necessary to use more realistic models for the radial distribution of magnetic fields that take into account the variations in the solar magnetic field cycle. Our attention thus has been directed to a detailed description of the observed solar magnetic field distribution and cycle variation, to create a model of the magnetic field radial distribution and cycle variations from 1 R_s to 1 AU. We then compare the magnetic fields derived using our model with the field measured at different times and distances, as well as with magnetic field profiles from previous models. The article will summarize the most recent models and results on magnetic field measurements.

The article is organized as follows. The data are described in Section 2. In Section 3, the photospheric and interplanetary magnetic field distribution and cycle evolution are presented, and a new model of the magnetic field calculation at different distances from the Sun with the consideration of solar cycle variations is suggested. The magnetic fields measured

by different methods are compared with the field calculated using our model in Section 4. The comparison of our model results with those derived using previous models is made in Section 5. The results are discussed in Section 6. The main results are listed in Section 7.

2. Data

Data on the large-scale photospheric magnetic field from the Wilcox Solar Observatory (WSO) were used for 1976 – 2015. Full-disk synoptic maps span a full Carrington rotation (1 CR = 27.2753 days). They are assembled from individual magnetograms that were observed during a solar rotation. The WSO synoptic maps only represent the radial component of the photospheric field (derived from observations of the line-of-sight field component by assuming the field to be approximately radial). The entire dataset consists of 530 synoptic maps and covers CRs 1642 – 2172 (June 1976 – December 2015). Synoptic map magnetic-field data consist of 30 data points in equal steps of sine latitude from $+70°$ to $-70°$. As the solar magnetic fields are measured from Earth, the field above 70° in the north and south hemispheres is not resolved. The longitude is presented in 5° intervals (Duvall *et al.*, 1977; Hoeksema and Scherrer, 1986).

WSO polar field observations were used in this study. The Sun's polar magnetic field strength is measured in the polemost 3' apertures each day at the WSO in the north and south hemispheres. The line-of-sight magnetic field between about $\pm 55°$ and the pole in the corresponding hemisphere is measured. The daily polar field measurements are averaged every 10 days in a centered 30-day window. The solar coordinates of the apertures shift and the square aperture at the pole is oriented differently on the Sun during each measurement due to the Earth motion above and below the solar equator each year.

Data on the IMF were obtained from the database called multi-source Operating Missions as a Node on the Internet (OMNI 2: King and Papitashvili, 2005). From the OMNI 2 database, the hourly mean values of the IMF measured by various spacecraft near the Earth orbit were taken. Only the radial component, B_X, of the OMNI 2 IMF was used in this study.

3. Large-Scale Photospheric and Coronal Magnetic Field Variations in Cycles 21 – 24

To study the variations in the magnetic field distribution in the solar corona, we have used the direct observations of the large-scale non-polar ($\pm 55°$) and polar (from 55° N to 90° N and from 55° S to 90° S) photospheric magnetic fields, which are the visible manifestations of the cyclic changes in the toroidal and poloidal components of the global magnetic field of the Sun. In addition to the general magnetic field distribution, occasional displacements and oscillations appear in localized regions of the solar corona due to the magnetic fields caused by CMEs, flows from coronal holes, flares, *etc*. Therefore, CR-averaged data were used.

To describe the non-polar magnetic field cycle variations, we created diagrams of the photospheric magnetic field distribution based on the observed large-scale photospheric magnetic fields from 55° S to 55° N latitude through Cycles 21 – 24. Figure 1a shows the longitudinal time-space distribution of the large-scale photospheric magnetic fields. The smoothed photospheric magnetic field longitudinal distribution is presented in Figure 1b. The CR-averaged distribution of positive- and negative-polarity IMF at Earth's orbit is shown in

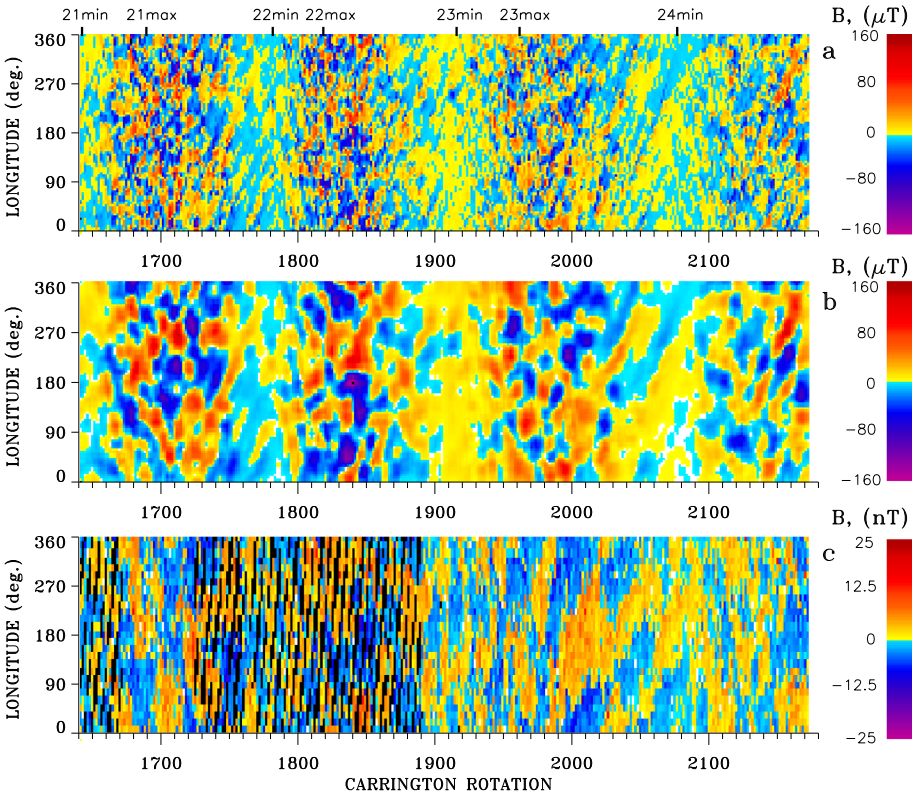

Figure 1 Longitudinal diagrams. (**a**) Large-scale photospheric magnetic fields. (**b**) Large-scale photospheric magnetic fields smoothed in 7 × 7 CRs. (**c**) IMF at 1 AU. *Red* denotes the positive-polarity magnetic fields, *blue* denotes the negative-polarity magnetic fields. *Black* denotes the missing data. The maxima and minima of Cycles 21 – 24 are marked *at the top*.

Figure 1c. The longitudinal diagrams were created in a CR-rotation system. The x-axes denote the date of 0° CR longitude at the central meridian, and the y-axes denote the longitude in each CR magnetic-field diagram. A detailed description of the magnetic field longitudinal diagram creation and solar global magnetic field evolution is given in Bilenko (2012) and Bilenko (2014). The maxima and minima of the cycles are marked at the top of Figure 1. Figure 1 demonstrates the close connection of the magnetic field direction and strength variations of the IMF at Earth's orbit and the photospheric magnetic fields.

Figure 2a shows the cycle changes in the photospheric large-scale magnetic field obtained from the longitudinal distribution of the photospheric magnetic fields by averaging over the latitude from 55 S to 55 N for every CR displayed in Figure 1a. Black denotes the positive- and negative-polarity photospheric magnetic fields, and light blue denotes the sum of their absolute values. Thin lines show changes in the CR-averaged magnetic fields, and thick lines correspond to the seven CR-averaged data. The maxima and minima of Cycles 21 – 24 are marked at the top of Figure 2. Examination of Figures 1 and 2 shows that the magnetic field does not change smoothly from the minimum of solar activity to the maximum, but in the form of some impulses. These changes reflect cyclical changes in the structure and strength of the solar global magnetic field (Bilenko, 2012, 2014; Bilenko and Tavastsherna, 2016). The maximum of the magnetic field magnitudes decreased, and it was highest in Cycle 21

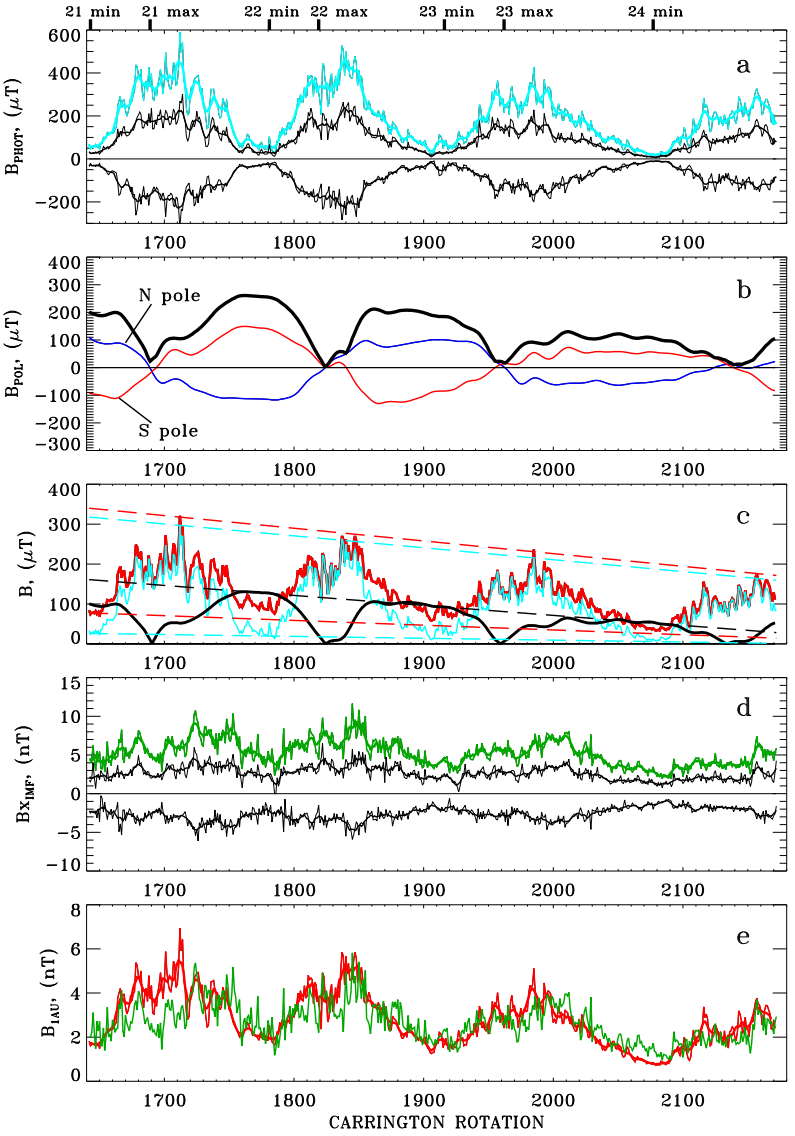

Figure 2 (**a**) Photospheric non-polar magnetic fields from the longitudinal diagram in Figure 1a. *Black* denotes the positive- and negative-polarity photospheric magnetic fields, and *light blue* denotes the sum of their absolute values. (**b**) CR-averaged polar magnetic field cycle variations at the north (N) and south (S) poles, and the sum of their absolute values (*black line*). (**c**) Sum of the positive- and negative-polarity photospheric (non-polar) magnetic fields (*light blue line*) from *panel (a)* and the sum of the north and south pole magnetic fields (*black line*) from *panel (b)*. The *red line* denotes the sum of polar and non-polar magnetic fields. (**d**) IMF measured at 1 AU. *Black* denotes the CR-averaged positive- and negative-polarity magnetic fields, and *green* denotes the sum of their absolute values. (**e**) The *red line* denotes the magnetic field at 1 AU calculated from Equation 4 as the sum the non-polar and polar magnetic fields. The *green line* denotes half of the sum of the CR-averaged positive- and negative-polarity IMF at 1 AU. In *panels (a)*, *(c)*, *(d)*, and *(e)* the *thin lines* correspond to CR-averaged and the *thick lines* to seven CR-averaged data. The maxima and minima of Cycles 21 – 24 are marked *at the top*. The straight lines in *panel c* are described in the text.

and lowest in Cycle 24. The magnetic field strength decrease can be given by

$$B_{\max}(t) = 317.82 - 0.30 \times t_{\mathrm{CR}}, \tag{1}$$

where t_{CR} is the time scale for the magnetic field calculation (the x axis units are in CRs) for the magnetic field calculation.

The minimum values of the magnetic field during solar activity minima also decreased from Cycle 21 to Cycle 24, and it was also highest in Cycle 21 and lowest in Cycle 24. We find a regression line

$$B_{\min}(t) = 26.17 - 0.47 \times t_{\mathrm{CR}}. \tag{2}$$

Such cyclic changes in magnetic fields (Figure 2a) reflect the time evolution of the toroidal component of the solar global magnetic field. This means that the toroidal component decreases from Cycle 21 to 24.

Magnetic field cycle variations at the solar poles are the observational manifestation of the poloidal component of the solar global magnetic field. Figure 2b shows CR-averaged magnetic field variations in the north (blue line) and south (red line) poles. The black line denotes the sum of their absolute values. The polar magnetic fields at the north and south poles diminished from Cycle 21 to 24. The cyclic changes in magnetic field (Figure 2b) reflect the time evolution of the poloidal component of the solar global magnetic field from Cycle 21 to 24. This means that both components have decreased from Cycle 21 to 24. The decrease in the polar magnetic field can be expressed by

$$B_{\mathrm{pol}}(t) = 161.04 - 0.25 \times t_{\mathrm{CR}}. \tag{3}$$

The magnetic field in the ecliptic plane can be modeled as the superposition of the toroidal and poloidal component cycle variations. The toroidal component dominates at solar maxima, and the influence of the poloidal component increases during solar minima. The toroidal component increases during solar maxima because of the enhancement of the active region magnetic fields. At solar minima, about 60% of the solar sphere above 2 R_{s} is dominated by polar coronal holes. The total magnetic field strength can therefore be determined as the sum of the non-polar photospheric magnetic fields (toroidal component of the solar global magnetic field, Figure 2a) and the polar magnetic field (poloidal component) obtained from Figure 2b. The non-polar (light blue line) and polar (black line) magnetic field components and their sum (red line) are shown in Figure 2c. We detect the magnetic field components that directly influence the measured IMF at Earth's orbit. It is assumed that the corona is in a steady state from 1 R_{s} to 1 AU. The non-polar and polar fields are observed in the ecliptic plane from Earth, therefore we can derive the radial component (B_{x}) of the IMF from the observed non-polar and polar photospheric magnetic field strength in the ecliptic plane using the relation

$$B(t,r) = \left(\frac{B_{\mathrm{phot+}}(t) + B_{\mathrm{phot-}}(t)}{2} + \frac{B_{\mathrm{pol}}(t)}{2} \right) \times \left(\frac{1}{r} \right)^2, \tag{4}$$

where $B_{\mathrm{phot+}}$ and $B_{\mathrm{phot-}}$ are averaged over the latitude from 55 S to 55 N. The absolute values of the positive- and negative-polarity magnetic fields at the photosphere derived from Figure 1a and shown in Figure 2a for each CR represent the toroidal component of the solar magnetic field. B_{pol} is the average of the sum of the observed unsigned north and south polar magnetic fields calculated for each CR (Figure 2b), and this represents the poloidal component of the solar global magnetic field. r is the distance from the center of the Sun in units of

the solar radius. The different behavior of polar and non-polar magnetic fields is also known from the cycle evolution of active region (Zharkov, Gavryuseva, and Zharkova, 2007) and coronal holes (Lowder, Qiu, and Leamon, 2017; Bilenko and Tavastsherna, 2016). Polar and non-polar magnetic fields represent the different components of the solar global magnetic field. Their cycle evolution is different. Therefore, they were included in Equation 4 as separate components.

As noted above, the magnitudes of the toroidal and poloidal magnetic field components of the solar global magnetic field decreased from Cycle 21 to Cycle 24. We find a regression line for our model (Equation 4) magnetic field cycle maxima

$$B_{\mathrm{m_{max}}}(t) = 339.93 - 0.32 \times t_{\mathrm{CR}}, \tag{5}$$

while the expression for the minima can be written as

$$B_{\mathrm{m_{min}}}(t) = 77.67 - 0.12 \times t_{\mathrm{CR}}. \tag{6}$$

In Figure 2c the dashed lines are the regression lines derived in Equations 1, 2, 3, 5, and 6.

Figure 2d shows the variation of the observed B_{x} component of the IMF at Earth's orbit. Black denotes the CR-averaged positive- and negative-polarity magnetic fields, and green denotes the sum of their absolute values. Thin lines show the CR-averaged IMF, and thick lines correspond to the seven CR-averaged data.

In Figure 2e the magnetic field derived at 1 AU using our model (Equation 4) is shown in red. The green line denotes the half of the sum of CR-averaged positive- and negative-polarity IMFs at 1 AU in Cycles 21 to 24. CR-averaged magnetic fields were compared. The magnetic fields retrieved from the photospheric and interplanetary magnetic fields measured at Earth's orbit were calculated the same way. In Equation 4, the magnetic fields were used as half of the sum of the absolute values of positive- and negative-polarity non-polar and polar magnetic fields averaged during each CR. Likewise, the IMF is also the sum of CR-averaged of the absolute values of the positive- and negative-polarity B_{x} component of the IMF divided by 2. Figure 2e shows that our model fits the B_{x} component of the IMF at 1 AU very well, particularly during Cycles 23 and 24. From a comparison of the magnetic fields as observed and calculated from our model, we conclude that our model magnetic field strength variation adequately explains the main features of the IMF changes during Cycles 21 to 24. However, there are certain differences. The difference is greater during the maximum phase in Cycle 21, but the mismatch is significantly weaker in the maxima of Cycles 22 and 24 (Figure 2e). Some peaks in magnetic fields derived using our model (Equation 4) coincide with peaks in the IMF, and some peaks follow the peaks in the IMF. The coincidence between the IMF and our model-predicted magnetic fields at 1 AU is more pronounced during the declining phases. The reduction of the misalignment between the interplanetary magnetic field and the field predicted using our model observed from Cycle 21 to Cycle 24 can be explained by the fact that the quality of observations and measurements of both IMF and solar magnetic fields has significantly improved by now. We have also carried out a correlation analysis of our results in order to quantify the agreement. The correlation coefficients between the observed IMF and magnetic fields at 1 AU predicted by our model were calculated. The modeled CR-averaged magnetic fields correlate with the IMF at Earth's orbit with a coefficient of 0.691. The correlation between seven CR-averaged calculated magnetic fields and seven CR-averaged B_{x} components of the IMF reaches 0.81. For Cycles 21 to 24, the modeled CR-averaged magnetic field correlates with the CR-averaged B_{x} component of the IMF at Earth's orbit with coefficients of 0.42, 0,70,

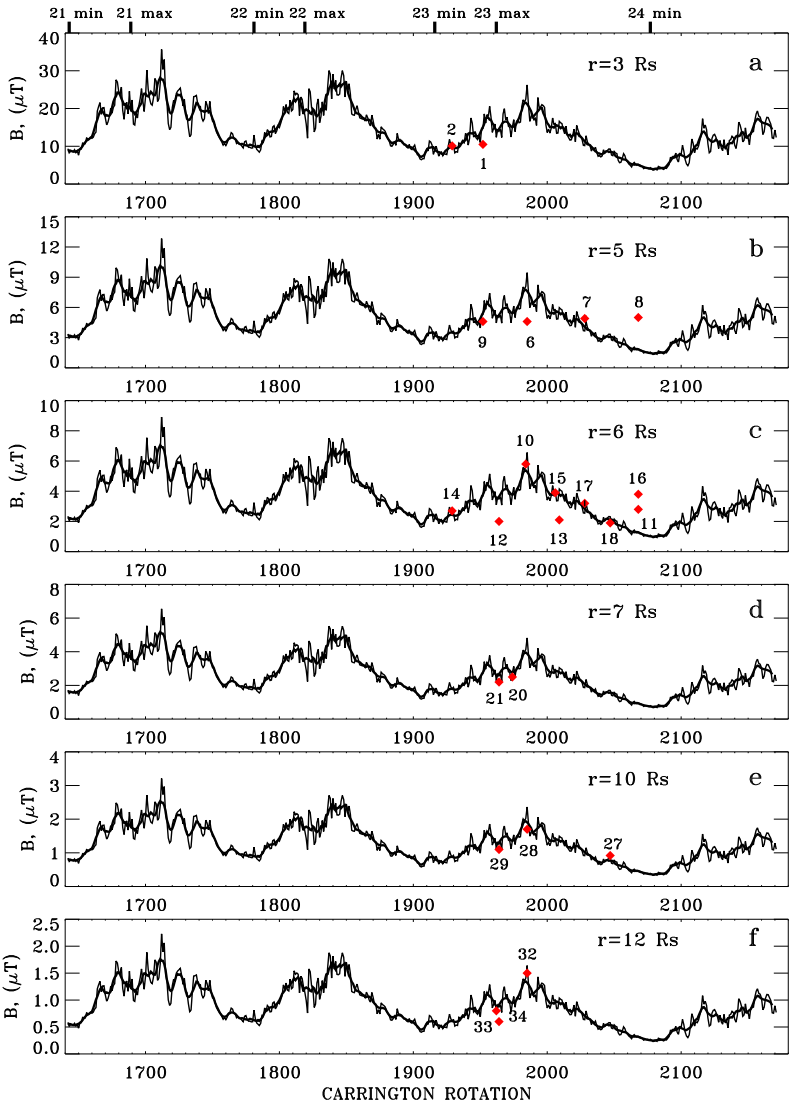

Figure 3 Model calculated magnetic fields at 3 R_s, 5 R_s, 6 R_s, 7 R_s, 10 R_s, and 12 R_s. *Red points* denote the directly measured IMF (from Table 1) close to these distances. The *labels of the points* correspond to their number in Table 1. The maxima and minima of Cycles 21 to 24 are marked *at the top*.

0.74, and 0.75 and that for seven CR-averaged values with coefficients 0.52, 0,88, 0.85, and 0.89. Again, this implies a very good correlation. Our model, Equation 4, is shown to be a good representation of the measured radial, B_x, component of the IMF in the ecliptic plane.

Figures 3 and 4 show some examples of the modeled magnetic field evolution from Cycles 21 to 24 calculated at distances of 3 R_s, 5 R_s, 6 R_s, 7 R_s, 10 R_s, and 12 R_s (Figure 3), and 75 R_s, 80 R_s, 85 R_s, 90 R_s, 95 R_s, and 100 R_s (Figure 4). In Figures 3 and 4 we see that the magnetic field declines from $\approx$20 μT to $\approx$20 nT in the distance range from 3 R_s to 100 R_s. The magnetic field cycle variations derived for different distances and illustrated

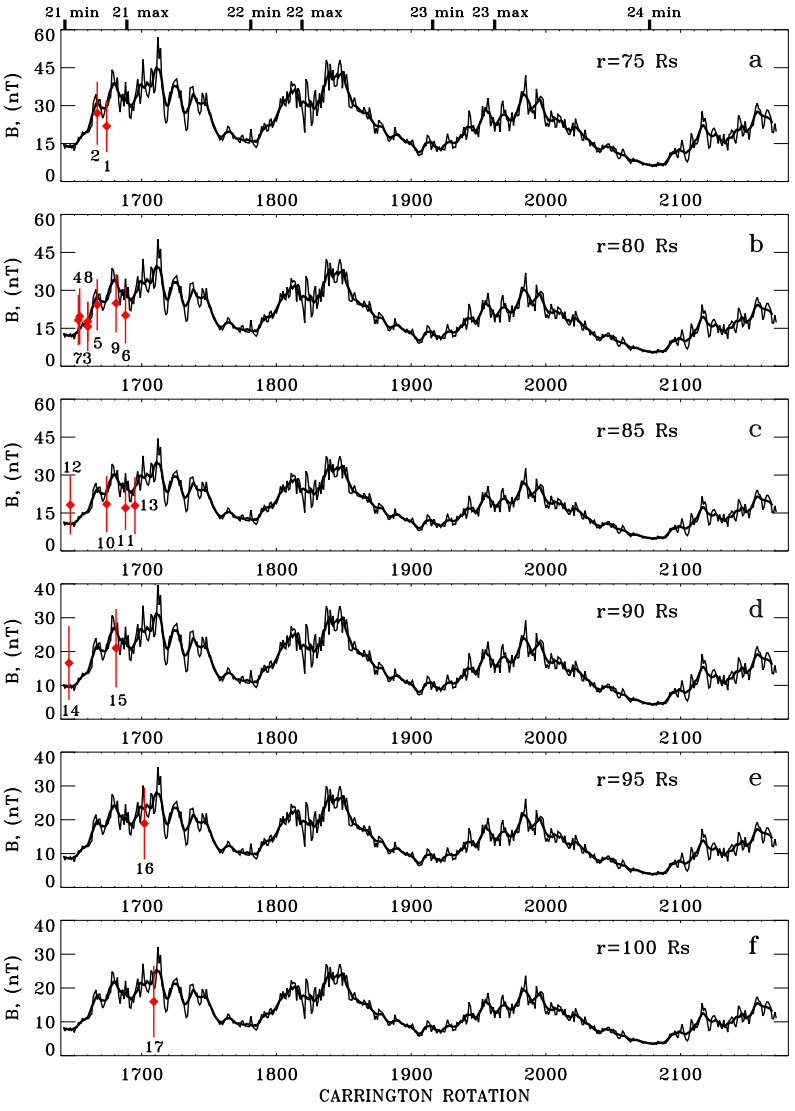

Figure 4 Modeled magnetic fields at 75 R_s, 80 R_s, 85 R_s, 90 R_s, 95 R_s, and 100 R_s. *Red points* denote the IMF measured by the *Helios 1* and *Helios 2* spacecraft from Table 2. The *labels of the points* correspond to their numbers in Table 2. The maxima and minima from Cycles 21 to 24 are marked *at the top*.

in Figures 3 and 4 should be regarded as a good approximation of the cycle behavior of the radial magnetic field profiles in the heliosphere. Thus, this method for calculating the magnetic field is a useful tool for describing the evolution of the solar corona and interplanetary large-scale magnetic field cycle at different distances from the Sun.

With our model, we can also derive the radial magnetic field strength profiles for different solar activity phases and for different distances from the Sun. Figure 5 shows the magnetic

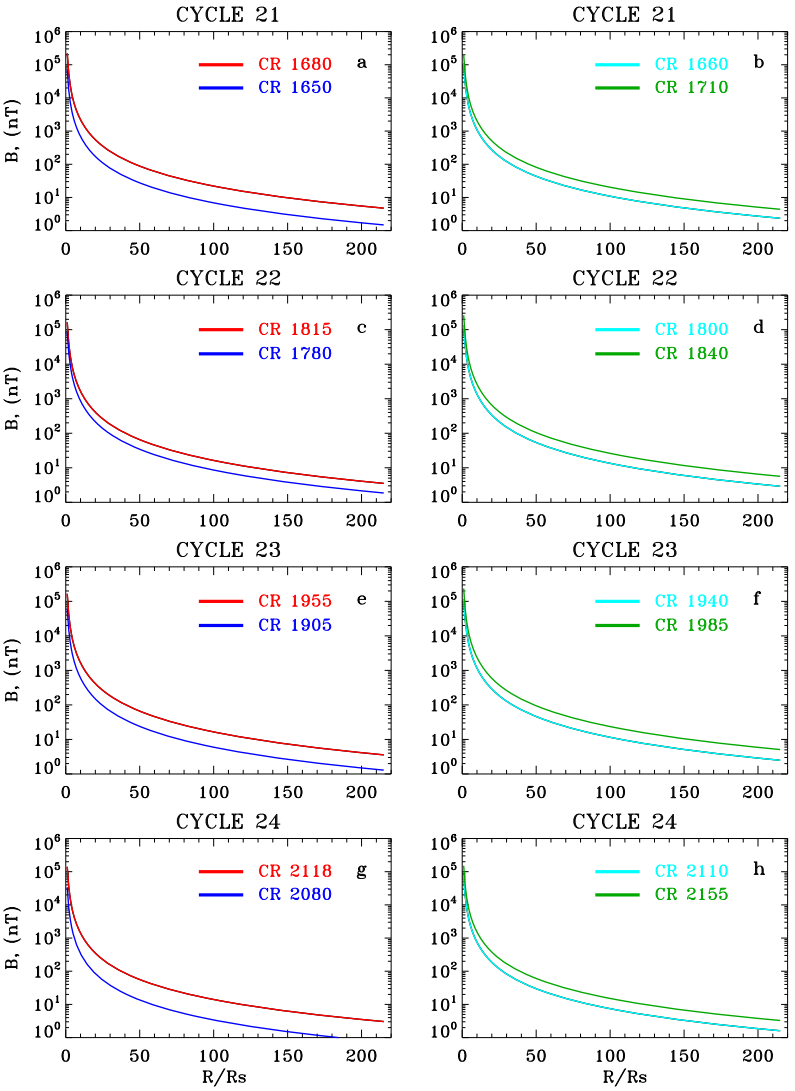

Figure 5 Magnetic field distributions calculated using our model (Equation 4) for different activity states of the corona. *In each panel*, some CRs are shown for different phases of solar activity. *Blue curves* denote the solar activity minimum corona, *red curves* correspond to the solar activity maximum corona, *light blue curves* denote solar corona at the rising phases, and *green curves* denote the solar corona at the declining phases.

field radial profiles from 1 R_s to 1 AU. The profiles were derived using Equation 4 as a function of distance for different phases of Cycles 21 to 24. The magnetic field profiles were calculated for different corona activity states: i) blue lines denote the solar activity minimum corona, ii) red lines correspond to the solar activity maximum corona, iii) light blue lines denote the solar corona at the rising phases, and iv) green lines denote the solar corona at the declining phases. In each panel, some CRs are shown for different phases of solar activity.

4. Coronal Magnetic Field Measurements in Cycles 21 to 24

Table 1 summarizes the observed magnetic fields (column 6) determined by different authors at different distances (column 4) from the Sun and those calculated using our model, Equation 4, (column 5) at the same distances and the same time (columns 2 and 3). The magnetic field measurements were taken from the articles cited in column 7.

Table 1 shows that the derived magnetic field values are consistent with other estimates in a similar distance range. In Figure 3 the calculated magnetic fields at 3 R_s, 5 R_s, 6 R_s, 7 R_s, 10 R_s, and 12 R_s are shown and compared to those measured. Red points denote the directly measured IMF (from Table 1) that is close to these distances. We conclude from this that our model adequately describes the observed magnetic fields. The comparison of the calculated magnetic field with the observations is complicated by the fact that many of the observations were made using different methods and using different solar corona plasma density models. Moreover, large-scale and small-scale irregularities, as well as flows of dense and rarefied plasma, move with different speeds in the solar corona and interplanetary space, creating regions of high and sparse density at different distances from the Sun. Even a cursory examination of the measured magnetic fields (Table 1, column 6) and cataloged in the literature (Table 1, column 7) shows a wide disparity between the determinations of various authors. In spite of the large scatter in the observations, we conclude that they are adequately reproduced by our model. Such a difference can also result from either calibration differences or the influence of different solar activity events. Observed and modeled magnetic fields differ also because it is hard to distinguish the enhanced magnetic fields, for example in a CME or a streamer region, from the background magnetic field. Our model determines the background radial distribution of the magnetic field strength and its cycle evolution. The difference in the measured magnetic fields can also result from the dependence of the magnetic field on the selected place of the observed events. Hariharan *et al.* (2014) estimated the magnetic field strength in the solar corona ahead of and behind the MHD shock front associated with a CME at a distance of $\approx 2\ R_s$. They found magnetic fields of $\approx (0.7-1.4) \pm 0.2$ G and $\approx (1.4-2.8) \pm 0.1$ G, respectively. Bemporad and Mancuso (2010) determined the plasma parameters of a fast CME-driven shock associated with the solar eruption of 22 March 2002. According to their study, the magnetic field undergoes a compression from a pre-shock value of ≈ 0.02 G up to a post-shock magnetic field of ≈ 0.04 G.

The *Helios* mission provides very good magnetic field observations. The observations performed by the *Helios 1* and *Helios 2* spacecraft allow monitoring the IMF conditions in the inner heliosphere from 0.3 to 0.6 AU. We also compare the calculated magnetic field strength (Equation 4) with *in situ* measurements made by the *Helios 1* and *Helios 2* spacecraft (Villante, Mariani, and Cirone, 1982).

In Table 2 we list the hourly averages of the observed unsigned IMF radial component measured by the *Helios 1* (H1) and *Helios 2* (H2) (column 2) spacecraft (column 8, from Villante, Mariani, and Cirone, 1982). Magnetic fields in column 7 were calculated using our model (Equation 4) at the same distances (columns 5, 6) and time (columns 3, 4) as in Villante, Mariani, and Cirone (1982). The calculated magnetic fields at 75 R_s, 80 R_s, 85 R_s, 90 R_s, 95 R_s, and 100 R_s are shown in Figure 4. Red points denote the IMF measured by the *Helios 1* and *Helios 2* spacecraft from Table 2. The agreement between our model predictions and those derived from direct *in situ* measurements is quite satisfactory. From a comparison of Figures 2, 3, 4, and 5 and Tables 1 and 2 of the different magnetic field values as observed and calculated from our model (Equation 4), we conclude that our model adequately explains the main features of the magnetic field at different distances from the Sun during different cycle phases. Therefore, the comparison of the observed magnetic

Table 1 Observed magnetic fields and fields calculated using our model at the same distances from the Sun and the same time. R is the distance from the Sun.

N	Date	CR	R (R_S)	B calc. (μT)	B obs. (μT)	References
1	2	3	4	5	6	7
1	25-Jul-1999	1952	3.08	13.99	10.5	Kim *et al.* (2012)
2	14-Nov-1997	1929	3.33	7.86	10.1	Kim *et al.* (2012)
3	24-Oct-2003	2009	3.56	11.79	5.6	Kim *et al.* (2012)
4	1-Apr-2001	1974	4.21	7.70	5.2	Kim *et al.* (2012)
5	22-Mar-2002	1987	4.3	8.09	1.9	Bemporad and Mancuso (2010)
6	14-Jan-2002	1985	4.82	10.17	4.6	Kim *et al.* (2012)
7	Mar – Apr-2005	2028	5.0	3.66	4.6 – 5.2	Ingleby, Spangler, and Whiting (2007)
8	25-Mar-2008	2068	5.0	1.87	5.0	Gopalswamy and Yashiro (2011)
9	25-Jul-1999	1952	5.55	4.31	4.6	Kim *et al.* (2012)
10	28-Dec-2001	1984	5.98	5.66	5.8	Kim *et al.* (2012)
11	5-Apr-2008	2068	6.0	1.3	2.8	Poomvises *et al.* (2012)
12	15-Jun-2000	1964	6.06	3.42	2.0	Kim *et al.* (2012)
13	24-Oct-2003	2009	6.10	4.02	2.1	Kim *et al.* (2012)
14	14-Nov-1997	1929	6.19	2.27	2.7	Kim *et al.* (2012)
15	16-Aug-2003	2006	6.2	3.75	3.9	Spangler (2005)
16	25-Mar-2008	2068	6.2	1.22	3.8	Gopalswamy and Yashiro (2011)
17	Mar – Apr-2005	2028	6.2	2.38	3.0 – 3.4	Ingleby, Spangler, and Whiting (2007)
18	28-Aug-2006	2047	6.2	2.17	1.9	You *et al.* (2012)
19	5-May-2000	1962	6.35	2.76	3.5	Kim *et al.* (2012)
20	1-Apr-2001	1974	6.69	3.05	2.5	Kim *et al.* (2012)
21	15-Jun-2000	1964	7.11	2.49	2.2	Kim *et al.* (2012)
22	29-Aug-2005	2033	7.5	1.39	2.7	You *et al.* (2012)
23	14-Jan-2002	1985	7.78	3.90	2.3	Kim *et al.* (2012)
24	4-May-2000	1962	7.92	1.78	1.8	Kim *et al.* (2012)
25	25-Jul-1999	1952	8.50	1.84	3.4	Kim *et al.* (2012)
26	5-May-2000	1962	9.06	1.36	2.1	Kim *et al.* (2012)
27	30-Aug-2006	2047	9.9	0.85	0.92	You *et al.* (2012)
28	14-Jan-2002	1985	10.06	2.33	1.7	Kim *et al.* (2012)
29	15-Jun-2000	1964	10.31	1.18	1.1	Kim *et al.* (2012)
30	4-Apr-2000	1961	11.46	1.09	2.0	Kim *et al.* (2012)
31	25-Jul-1999	1952	11.7	0.97	2.1	Kim *et al.* (2012)
32	14-Jan-2002	1985	12.16	1.59	1.5	Kim *et al.* (2012)
33	15-Jun-2000	1964	12.27	0.83	0.6	Kim *et al.* (2012)
34	4-May-2000	1962	12.64	0.7	0.8	Kim *et al.* (2012)
35	28-Dec-2001	1984	14.89	0.91	1.6	Kim *et al.* (2012)
36	4-Apr-2000	1961	15.33	0.609	1.0	Kim *et al.* (2012)
37	5-Apr-2008	2068	120.0	0.003	0.017	Poomvises *et al.* (2012)

Table 2 Magnetic fields observed with *Helios 1* (H1) and *Helios 2* (H2), and those calculated using our model at the same distances from the Sun and the same time.

N	Spacecraft	Perihelios	*CR*	*R* R_{AU}	*R* (R_s)	*B* calc. (nT)	*B* obs. (nT)
1	2	3	4	5	6	7	8
1	H2	2-Nov-1978	1674	0.354	76.11	31.17	21.9 ± 10.3
2	H2	30-Apr-1978	1667	0.356	76.54	28.39	27.0 ± 12.5
3	H2	26-Oct-1977	1660	0.362	77.83	17.97	17.7 ± 7.8
4	H2	23-Apr-1977	1654	0.372	79.98	14.86	19.7 ± 11.1
5	H1	29-Apr-1978	1667	0.373	80.195	25.86	24.3 ± 10.1
6	H2	9-Nov-1979	1688	0.375	80.625	34.03	20.2 ± 11.2
7	H1	13-Apr-1977	1653	0.381	81.915	14.50	18.3 ± 9.9
8	H1	21-Oct-1977	1660	0.387	83.205	15.72	15.7 ± 9.7
9	H2	7-May-1979	1681	0.389	83.635	30.62	24.9 ± 11.5
10	H1	5-Nov-1978	1674	0.394	84.71	25.16	18.5 ± 11.1
11	H1	21-Nov-1979	1688	0.394	84.71	30.83	17.0 ± 8.7
12	H2	19-Oct-1976	1647	0.396	85.14	11.31	$18.2 \pm 11,7$
13	H1	29-May-1980	1695	0.398	85.57	25.45	17.9 ± 11.3
14	H1	5-Oct-1976	1646	0.406	87.29	10.10	16.6 ± 10.9
15	H1	14-May-1979	1681	0.418	89.87	26.52	21.0 ± 11.6
16	H1	5-Jan-1980	1702	0.438	94.17	25.54	18.9 ± 10.6
17	H1	13-Jun-1981	1709	0.469	100.835	19.35	16.0 ± 10.6

fields with those predicted by our model shows that the magnetic field in the heliosphere is determined by the cycle variations of the sum of the poloidal and toroidal components of the solar global magnetic field.

5. Coronal Magnetic Field Models

Magnetic field measurements are important for testing coronal magnetic field models. Magnetic field models have played a very important role in the interpretation of different solar activity phenomena and in the study of outward-flowing coronal material into interplanetary space. In this section, we first summarize various models for deriving the magnetic field radial distribution. The models discussed below are presented in the form of functions in Figure 6. When we assume conservation of the magnetic flux in interplanetary space, the magnetic field can be continued to arbitrary radial distances, r, from the Sun (Parker, 1958) by

$$B(r) = B_s \times \left(\frac{R_s}{r}\right)^2, \tag{7}$$

where B_s is the magnetic field at the photosphere, obtained using some measurements and assumptions (*e.g.* Mann *et al.*, 1999), or is composed of the field of an active region and that of the quiet Sun (Warmuth and Mann, 2005), R_s is the radius of the Sun, and r is the distance from the center of the Sun in units of the solar radius.

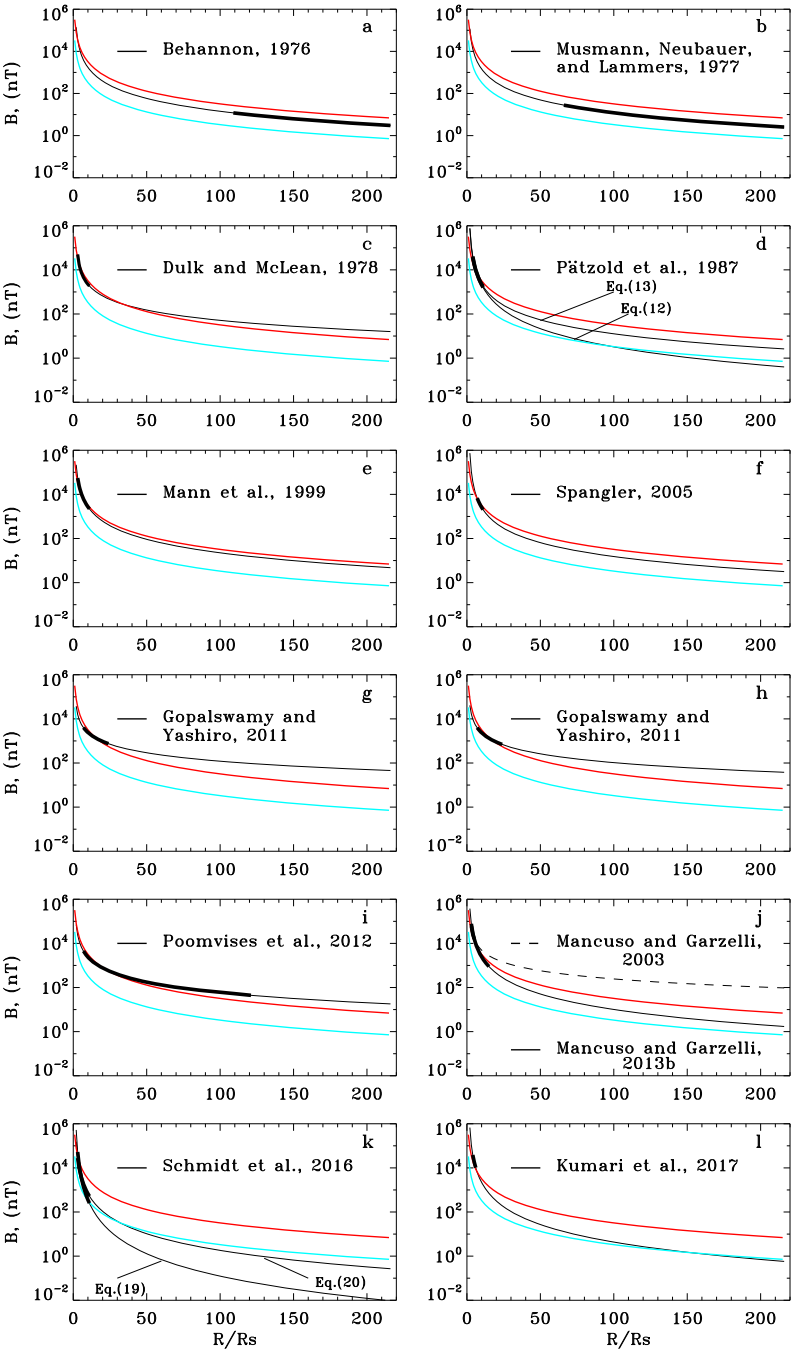

Figure 6 Magnetic field distributions from 1 R_S to 1 AU calculated for different models (*thin black profiles*). *Thick black lines* denote the part of the profiles marking the distances for which the models were developed by their authors. *Red profiles* denote the distribution of magnetic fields using our model for the maximum of Cycle 21 (CR 1712). *Blue profiles* denote the distribution of magnetic fields using our model for the minimum of Cycle 24 (CR 2079).

The radial profile of the magnetic field can also be represented by an empirical formula of the form

$$B(r) = K \times r^{-\alpha}, \tag{8}$$

where K and α are coefficients derived from some approximation of different measurements or models, and r is the distance from the center of the Sun in units of the solar radius. A significant number of models were created based on Equation 8 (*e.g.* Dulk and McLean, 1978; Pätzold *et al.*, 1987; Mancuso *et al.*, 2003; Gopalswamy and Yashiro, 2011). Many models have used Equation 8 formally, as a mathematical approximation only. The magnetic field values are not used in these equations.

Traditionally, the problem of a radial magnetic field distribution has been solved by combining the data obtained using different observations of magnetic fields measured at different times with different methods and at different distances from the Sun with instrumentation onboard different spacecraft. Then, the observations are summarized in one curve and fitted by a function like Equations 7 and 8. Such models only depend on r. They do not reflect the actual distribution and cycle evolution of magnetic fields.

Figure 6 summarizes the radial magnetic field distributions calculated using different models. The profiles were computed for radial distances from 1 R_s to 1 AU (thin black profiles). Thick black lines denote the part of the profiles that marks the distances for which the models were developed by their authors. For comparison, the radial magnetic field profiles calculated using our model are also shown in Figure 6. The magnetic field radial profiles corresponding to the maximum and minimum solar cycle phases are included. Red lines denote the radial distribution of magnetic fields calculated using our model for the maximum of Cycle 21 (CR 1712). Blue lines denote the radial distribution of magnetic fields calculated using our model for the minimum of Cycle 24 (CR 2079). These modeled profiles were calculated from the observed photospheric magnetic fields for the highest and the lowest solar activity. Therefore, they determine the range of profiles that are possible at different levels of the solar activity, and they can be used for the estimation of different models.

Using measurements of the IMF from several different spacecraft, Behannon (1976) showed that the radial component of the magnetic field between 0.5 AU and 5 AU can be fitted by the function

$$B(r) = 3.0 \times 10^{-5} \left(\frac{r}{216} \right)^{-2}, \tag{9}$$

where $B(r)$ is in G and r is the distance from the center of the Sun in units of the solar radius (Figure 6a).

Musmann, Neubauer, and Lammers (1977) derived a similar expression for the radial variation of the IMF between 0.3 AU and 1.0 AU from *Helios 1* data during solar minimum

$$B(r) = 1.18 \times 10^{-4} r^{-2}, \tag{10}$$

where $B(r)$ is in T, and r is in units of the solar radius (Figure 6b).

One of the most frequently used models is the empirical formula proposed by Dulk and McLean (1978). These authors concentrated their attention on the magnetic field above active regions. Using different techniques and different observational data, they proposed an empirical single-parameter formula to calculate the radial profile of the magnetic field from 1.02 to 10 r/R_s

$$B(r) = 0.5 \times \left(\frac{r}{R_s} - 1 \right)^{-1.5}, \tag{11}$$

where $B(r)$ is in G, R_s is the solar radius, and r is in units of the solar radius (Figure 6c). They pointed out that the magnetic field in the corona can vary from one active region to another by an order of magnitude and that Equation 11 is consistent with the different data used within a factor of about three.

Pätzold *et al.* (1987) derived the mean coronal magnetic field from Faraday rotation measurements for $3 \leq r \leq 10\ R_s$ during solar minimum in 1975 – 1976 (Figure 6d, Equation 12),

$$B(r) = 7.9 \times 10^{-4} r^{-2.7}. \tag{12}$$

The magnetic field profile derived using a fit to the Faraday rotation data with a dipole term and an interplanetary term is given by (Figure 6d, Equation 13)

$$B(r) = \left(6r^{-3} + 1.18r^{-2}\right) \times 10^{-4}, \tag{13}$$

where $B(r)$ is in T, and r is in units of the solar radius. Clearly, our model profile is closer to that of Pätzold *et al.* (1987) in Equation 13 than to that of Pätzold *et al.* (1987) in Equation 12. The profile of Pätzold *et al.* (1987) in Equation 12 agrees well with our model for solar maximum at shorter distances, but it is lower than our model for solar minima.

Mancuso and Spangler (2000) and Spangler (2005) proposed a method for deriving the strength and spatial structure of the solar coronal magnetic field using observations of the Faraday rotation of radio sources (radio galaxy) occulted by the solar corona at heliocentric distances of 6 – 10 R_s (Figure 6f)

$$B(r) = 0.06\left(\frac{r}{R_1}\right)^{-3} + 3.1\left(\frac{r}{R_1}\right)^{-2}, \tag{14}$$

where $B(r)$ is in nanoTesla, R_1 is 1 AU, and r is the distance from the Sun in units of the solar radius. In this model, the field changes polarity at the coronal neutral line (Spangler, 2005).

Several models of the magnetic field radial distribution were based on CME observations. Gopalswamy and Yashiro (2011) determined the coronal magnetic field strength using white-light coronagraph measurements of the shock standoff distance and the radius of curvature of the flux rope during the 25 March 2008 CME. They showed that the radial profile of the magnetic field can be represented by a power law of the form

$$B(r) = p \times r^{-q}, \tag{15}$$

where $B(r)$ is in G, r in units of R_s, and p and q are the coefficients that depend on the plasma density model. Using the Saito (1977) density model with $\gamma = 4/3$ and for distances $> 9\ R_s$, they obtained $p = 0.377$ and $q = 1.25$ (Figure 6g). Using the Leblanc, Dulk, and Bougeret (1998) density radial-distribution model, they obtained $p = 0.409$ and $q = 1.3$ (Figure 6h). The Gopalswamy and Yashiro (2011) model extrapolation results in a slightly flatter magnetic field profile than that from our model. The modeled profiles reported by Gopalswamy and Yashiro (2011) agree with our model profiles at shorter distances, but the difference increases with distance. They determined the coronal magnetic field strength at a heliocentric range of 6 – 23 solar radii.

Following the standoff-distance method, Poomvises *et al.* (2012) derived the radial magnetic field strength in the heliocentric distance range from 6 to 120 R_s using data from the *Coronagraph 2* and *Heliospheric Imager I* instruments on board the STEREO spacecraft. They found that the radial magnetic field strength decreases from 28 mG at 6 R_s to

0.17 mG at 120 R_s. They derived magnetic field profiles in the form of Equation 15. Using the Saito (1977) density model and $\gamma = 4/3$, they obtained $p = 845.870$ and $q = 1.59$. Using the Leblanc, Dulk, and Bougeret (1998) density radial distribution model, they obtained $p = 706.383$ and $q = 1.54$. The coefficients are close in value, so that the resulting profiles coincide (Figure 6i).

Several models of the magnetic field radial distribution are based on solar radio emission analysis. Mann *et al.* (1999) have shown that coronal transient (or EIT) waves discovered by the *Extreme Ultraviolet Imaging Telescope (EIT)* on board the *SOHO* and coronal shock waves associated with type II radio bursts can be used to determine the magnetic field in the solar corona. They proposed a model of the radial magnetic field distribution for quiet regions at solar minimum

$$B(r) = 2.2 \times \left(\frac{R_s}{r}\right)^2, \tag{16}$$

where $B(r)$ is in G and r is in units of R_s (Figure 6e). They determined the magnetic field strength between $1.1 - 2.1$ solar radii. The model profile matches our estimates for the coronal magnetic field at solar maximum well.

Mancuso *et al.* (2003) studied the coronal plasma by analyzing type II radio bursts and SOHO/UVCS observations. The data sample comprises 37 metric type II radio bursts observed by ground-based radio spectrographs in 1999, during the rising phase of Cycle 23. The shock speeds were used to set upper limits to the magnetic field above active regions. An average functional form of the magnetic field estimates can be represented by the following radial profile, valid between about 1.5 and 2.3 R_s,

$$B(r) = (0.6 \pm 0.3) \times (r - 1)^{-1.2}, \tag{17}$$

where $B(r)$ is in G and r is in units of R_s (Figure 6j).

The coronal magnetic field can be inferred from band splitting of type II radio bursts (Vršnak *et al.*, 2002). Mancuso and Garzelli (2013a) have also analyzed the band splitting of type II radio bursts to determine the coronal magnetic field strength in the heliocentric distance range $\approx 1.8 - 2.9$ R_s. The same radial profile was obtained higher up in the corona by Mancuso and Garzelli (2013b) based on Faraday rotation measurements of extragalactic radio sources occulted by the solar corona as

$$B(r) = 3.76 \times r^{-2.29}, \tag{18}$$

where $B(r)$ is in G and r is in units of R_s (Figure 6j). The profiles derived describe the magnetic field in a range of heliocentric distances from 1.8 R_s to 14 R_s. Clearly, our model profile is more in line with the results of Mancuso and Garzelli (2013a) than with those of Mancuso *et al.* (2003).

The comparison of models developed by Behannon (1976), Musmann, Neubauer, and Lammers (1977), Pätzold *et al.* (1987) (Equation 13), Spangler (2005), and Mancuso and Garzelli (2013a) (Figure 6a, b, d (Equation 13), f, j) shows that the radial profiles derived from these models and those predicted by our model for the maximum and minimum corona states agree very well. The agreement is quite satisfactory, although it is impossible, based on the profiles, to prefer one model above the other.

Schmidt *et al.* (2016) derived the profile of the strength of the magnetic field in front of a CME-driving shock based on white-light images and the standoff-distance method. They also simulate the CME and its driven shock with a 3D MHD code. They found good

agreement between the two profiles (within $\pm 30\%$) between 1.8 and 10 R_s. The authors noticed that in their model the magnetic field profile is decreasing stronger than a monopolar (wind-like) magnetic field profile $\approx r^{-2}$ and a dipolar profile $\approx r^{-3}$ for an ideal spherically symmetric system. The magnetic field strength profile derived can be represented as

$$\lg\left(B_{\mathrm{calc}}(r)\right) = (-3.32 \pm 0.5) \times \lg(r) + (3.72 \pm 0.5) \tag{19}$$

and that simulated with the 3D MHD code

$$\lg\left(B_{\mathrm{sim}}(r)\right) = (-2.47 \pm 0.5) \times \lg(r) + (3.19 \pm 0.5), \tag{20}$$

where $B(r)$ is in mG and r is in units of R_s (Figure 6k). The profiles are similar to our model minimum profile at shorter distances, but the difference is growing rapidly with increasing distance.

Using radio and white-light observations, Kumari *et al.* (2017) have shown that a single power-law fit is sufficient to describe magnetic fields in the heliocentric distance range $\approx 2.5-4.5$ R_s,

$$B(r) = 6.7 \times r^{-2.6}, \tag{21}$$

where $B(r)$ is in G and r is in units of R_s (Figure 6l). The resulting profile matches our model profile for the magnetic field maximum at shorter distances and is close to our model profile for the magnetic field minimum at large distances.

Figure 6 shows that magnetic field profiles derived using different models are different. The difference in the magnetic field variation at 1 AU is one order of magnitude. The main difference between our model and the models described above is that they give only one value for one point at a certain distance from the Sun. They do not take into consideration the solar cycle magnetic field evolution. Our model gives more realistic magnetic field radial distributions that take into account the cycle variations of the solar toroidal and poloidal magnetic fields.

6. Discussion

In this article, we presented a new model for the radial B_x component of the IMF at various distances from the Sun during different solar cycle phases. The results show a rather good match between the measured B_x component of the IMF and the model predictions. The magnetic fields from the WSO were used in the study. However, it is known that the magnetic field measurements at different observatories are different. To compare data from different observatories, synoptic maps from the WSO, the Mount Wilson Observatory (MWO), Kitt Peak (KP), SOLIS, the SOHO/Michelson Doppler Imager (MDI), and the *Solar Dynamics Observatory* (SDO)/*Helioseismic and Magnetic Imager* (HMI) measurements of the photospheric field were analyzed by Riley *et al.* (2014), Virtanen and Mursula (2016, 2017). The comparison has shown that while there is a general qualitative agreement in the measured data, there are also some significant differences (Riley *et al.*, 2014). The observatories give a similar overall view of the solar magnetic field and the heliospheric current sheet evolution over the four last cycles. However, there are some periods when the data disagree (Virtanen and Mursula, 2016). The differences between the datasets can be due to instrument problems, the choice of the spectral lines that may be formed at different heights and may not measure the same magnetic field, and the measurement and treatment of polar fields. Furthermore for ground-based instruments, atmospheric turbulence can significantly degrade

the image quality. Another problem can be caused by different algorithms used to create synoptic maps (Riley *et al.*, 2014). This shows that the assumption that high-resolution maps from one observatory can be transformed into a lower-resolution map of another by simple averaging is strictly not true. Scaling factors are needed when comparing synoptic maps from different observatories. Therefore, conversion factors were computed by Riley *et al.* (2014) that relate measurements of different observatories using both synoptic map pixel-by-pixel and histogram-equating techniques. Virtanen and Mursula (2017) also proposed a method for scaling the photospheric magnetic field measurements based on a harmonic expansion. The benefit of the harmonic scaling method is that it can be used for datasets with different resolutions.

The WSO provides the longest and most homogeneous magnetic field observations; many investigations are based on WSO data. However, WSO provides the lowest values for the photospheric magnetic field data, *i.e.* a weaker coronal magnetic field strength than MWO, KP, SOLIS, SOHO/MDI, and SDO/HMI (Riley *et al.*, 2014). The size of a WSO pixel is 3 arcmin in sky coordinates, or 180 arcsec, which at disk center represents about 126 Mm, or about 10 deg of heliographic longitude. Such large pixels cannot resolve active regions, therefore most active region flux is not detected by WSO. This shows that the very low spatial resolution of WSO might explain part of the good match, because the origin of the IMF is the large-scale photospheric magnetic field (Ness and Wilcox, 1964, 1965, 1966; Severny *et al.*, 1970). The IMF evolves in response to the solar coronal and photospheric magnetic field at its base. The source of the interplanetary sector structure is associated with large-scale photospheric magnetic field patterns, *i.e.* the patterns of weak photospheric background fields (Wilcox, 1968, Wilcox and Ness, 1967) with an area equal to about one-fourth of the area of the solar disk (Scherrer and Wilcox, 1972); furthermore, according to Plyusnina (1985), the size of the unipolar photospheric magnetic field pattern is on average larger than 40°. Therefore, such a good coincidence between the measured magnetic field and that predicted by our model largely arises because of the low-resolution measurements of the WSO. The total flux of the active region is unresolved. The magnetic field measured at the WSO is the large-scale field that forms and governs the IMF.

The photospheric magnetic field and the IMF are measured from Earth and at Earth's orbit. Only the flux from different latitudes that is detected at Earth is considered. This does not imply that approximately the same proportion of low- and high-latitude fields contribute to the IMF B_x component. We do not see the real radial polar magnetic field from Earth. As the value of the polar magnetic field observed from Earth is used, not the full magnetic flux of the polar regions is really measured, but only the tangential component of the polar magnetic field of the visible polar area. The contribution of polar regions is far less than that of low-latitude fields, especially during maximum phases, when the polar region influence is negligible, despite the fact that the polar flux is much more unipolar than the low-latitude flux over most of the cycle. The role of polar fields increases during minimum phases. The central part of the visible solar disk contributes with a great amount of magnetic flux to the magnetic field measured at Earth. Scherrer *et al.* (1977) have shown that about half the contribution to the mean (Sun-as-a-star) field comes from the central 35% of the disk area.

The influence of active region magnetic fields on the IMF is insignificant beyond the source surface. It was found that the IMF originates in the large-scale photospheric magnetic fields. The source of the interplanetary sector structure is associated with the pattern of weak photospheric background fields (Wilcox, 1968). The background solar magnetic field is represented predominantly by a radial field (as seen from vector magnetograms and EUV images). We stress that it does not show significant variations with latitude. The independence of latitude was also observed by *Ulysses* in the radial component of the IMF (Forsyth

et al., 1996; Smith and Balogh, 1995; Balogh *et al.*, 1995). As described above, however, both the photospheric magnetic field and the IMF are measured from Earth and Earth's orbit. Hence, the contribution of the unipolar regions to the total magnetic flux that reaches Earth also mainly comes from the central solar region.

Finally, we note that the photospheric magnetic field must be accurately determined as it is used to calculate the coronal magnetic field and the IMF. The magnetic field measurements from other observatories can therefore be used with an appropriate scaling factor to calculate the IMF at various distances from the Sun during different cycle phases.

7. Conclusion

A new model has been proposed for the determination of the magnetic field at different distances from the Sun throughout solar cycles. The model depends on the observed large-scale photospheric magnetic fields. Direct observations of the large-scale non-polar photospheric ($\pm 55°$) and polar (from 55° N to 90° N and from 55° S to 90° S) magnetic fields were used, which are the visible manifestations of cyclic changes in the toroidal and poloidal components of the solar global magnetic field. The model magnetic field is determined as the sum of the non-polar photospheric magnetic field (toroidal component of the solar global magnetic field) and the polar magnetic field (poloidal component) cycle variations.

The agreement between our model predictions and magnetic fields derived from direct *in situ* measurements at different distances from the Sun and at different times is quite satisfactory. From a comparison of the magnetic fields as observed and as calculated from our model at 1 AU, we also conclude that the modeled variation in magnetic field strength adequately explains the main features of the IMF B_x component cycle evolution at Earth's orbit. The CR-averaged calculated magnetic fields correlate with the CR-averaged IMF B_x component at Earth's orbit with a coefficient of 0.691. The correlation between seven CR-averaged calculated magnetic fields with the IMF B_x component reaches 0.81. For Cycles 21 to 24, the model CR-averaged calculated magnetic fields correlate with a CR-averaged IMF B_x component at Earth's orbit with coefficients of 0.42, 0,70, 0.74, and 0.75, and the fields for seven CR-averaged values with coefficients of 0.52, 0,88, 0.85, and 0.89.

The variations in the magnetic field with the cycle that we derived for different distances should be regarded as a good approximation of the radial cycle behavior of the magnetic fields in the heliosphere. Thus, this method of magnetic field calculation is a useful tool for describing the solar corona and interplanetary large-scale magnetic field cycle evolution at different distances from the Sun. The model should be regarded as a good approximation of the cycle behavior of the magnetic field in the heliosphere.

The magnetic field profiles derived from our model are similar to those of empirical models and previous estimates. The main difference between our model and the models described in Section 5 is that they give only one value for one point at a certain distance from the Sun. They do not take into consideration the solar cycle evolution. Our model gives more realistic magnetic field radial distributions that take into account the cycle variations of the solar toroidal and poloidal magnetic fields.

A particularly interesting finding is the decrease in the maximum of the photospheric magnetic field magnitude from Cycle 21 to Cycle 24. We note that the minimum values of the magnetic field in the solar activity minima have also decreased from Cycle 21 to Cycle 24. The polar magnetic field also decreased. Such changes in magnetic fields reflect the time evolution of the toroidal and poloidal components of the solar global magnetic field. This means that both components, and therefore, the solar global magnetic field, decreased from Cycle 21 to Cycle 24.

Acknowledgements The author expresses her appreciation to the anonymous referee for a very thorough and helpful revision of the paper.

Wilcox Solar Observatory data used in this study were obtained via the web site http://wso.stanford.edu at 2018:03:11 01:13:34 PST courtesy of J.T. Hoeksema. The Wilcox Solar Observatory is currently supported by NASA.

Data on the IMF were obtained from multi-source OMNI 2 database via the web site https://omniweb.gsfc.nasa.gov/ow.html. The author thanks the GSFC/SPDF and OMNIWeb for the opportunity to use this data.

Disclosure of Potential Conflict of Interest The author declares to have no conflicts of interest.

References

Akhmedov, S.B., Gelfreikh, G.B., Bogod, V.M., Korzhavin, A.N.: 1982, The measurement of magnetic fields in the solar atmosphere above sunspots using gyroresonance emission. *Solar Phys.* **79**, 41. DOI.

Balogh, A., Smith, E.J., Tsurutani, B.T., Southwood, D.J., Forsyth, R.J., Horbury, T.S.: 1995, The heliospheric magnetic field over the South polar region of the Sun. *Science* **268**, 1007. DOI.

Banaszkiewicz, M., Axford, W.I., McKenzie, J.F.: 1998, An analytical solar magnetic field model. *Astron. Astrophys.* **337**, 940.

Behannon, K.W.: 1976, Mariner 10 interplanetary magnetic field results. In: Williams, D.J. (ed.) *Physics of Solar Planetary Environments*, *Proc. International Symp. on Solar—Terrestrial Physics* **1**, Am. Geophys. Union, Washington, 332.

Bemporad, A., Mancuso, S.: 2010, First complete determination of plasma physical parameters across a coronal mass ejection-driven shock. *Astrophys. J.* **720**, 130. DOI.

Bemporad, A., Susino, R., Frassati, F., Fineschi, S.: 2016, Measuring coronal magnetic field with remote sensing observations of shock waves. *Front. Astron. Space Sci.* **3**, 17. DOI.

Bilenko, I.A.: 2012, Formation of coronal mass ejections at different phases of solar activity. *Geomagn. Aeron.* **52**, 1005. DOI.

Bilenko, I.A.: 2014, Influence of the solar global magnetic-field structure evolution on CMEs. *Solar Phys.* **289**, 4209. DOI.

Bilenko, I.A., Tavastsherna, K.S.: 2016, Coronal hole and solar global magnetic field evolution in 1976–2012. *Solar Phys.* **291**, 2329. DOI.

Bogod, V.M., Stupishin, A.G., Yasnov, L.V.: 2012, On magnetic fields of active regions at coronal heights. *Solar Phys.* **276**, 61. DOI.

Bogod, V.M., Yasnov, L.V.: 2008, Vertical structure of the magnetic field in active regions of the Sun at coronal heights. *Cosm. Res.* **46**, 309. DOI.

Bogod, V.M., Yasnov, L.V.: 2016, Determination of the structure of the coronal magnetic field using microwave polarization measurements. *Solar Phys.* **291**, 3317. DOI.

Brosius, J.W., White, S.M.: 2006, Radio measurements of the height of strong coronal magnetic fields above sunspots at the solar limb. *Astrophys. J.* **641**, L69. DOI.

Cho, K.-S., Lee, J., Gary, D.E., Moon, Y.-J., Park, Y.D.: 2007, Magnetic field strength in the solar corona from type II band splitting. *Astrophys. J.* **665**, 799. DOI.

Dulk, G.A., McLean, D.J.: 1978, Coronal magnetic fields. *Solar Phys.* **57**, 279. DOI.

Duvall, T.L.J., Wilcox, J.M., Svalgaard, L., Scherrer, P.H., McIntosh, P.S.: 1977, Comparison of Ha synoptic charts with the large-scale solar magnetic field as observed at Stanford. *Solar Phys.* **55**, 63. DOI.

Forsyth, R.J., Balogh, A., Horbury, T.S., Erdoes, G., Smith, E.J., Burton, M.E.: 1996, The heliospheric magnetic field at solar minimum: ULYSSES observations from pole to pole. *Astron. Astrophys.* **316**, 287.

Gelfreikh, G.B., Peterova, N.G., Riabov, B.I.: 1987, Measurements of magnetic fields in solar corona as based on the radio observations of the inversion of polarization of local sources at microwaves. *Solar Phys.* **108**, 89. DOI.

Gibson, S.E., Bagenal, F.: 1995, Large-scale magnetic field and density distribution in the solar minimum corona. *J. Geophys. Res.* **100**, 19865. DOI.

Gopalswamy, N., Yashiro, S.: 2011, The strength and radial profile of the coronal magnetic field from the standoff distance of a coronal mass ejection-driven shock. *Astrophys. J. Lett.* **736**, L17. DOI.

Gopalswamy, N., Nitta, N., Akiyama, S., Mäkelä, P., Yashiro, S.: 2012, Coronal magnetic field measurement from EUV images made by the Solar Dynamics Observatory. *Astrophys. J.* **744**, 72. DOI.

Hariharan, K., Ramesh, R., Kishore, P., Kathiravan, C., Gopalswamy, N.: 2014, An estimate of the coronal magnetic field near a solar coronal mass ejection from low-frequency radio observations. *Astrophys. J.* **795**, 14. DOI.

Hoeksema, J.T., Scherrer, P.H.: 1986, An atlas of photospheric magnetic field observations and computed coronal magnetic fields: 1976 – 1985. *Solar Phys.* **105**, 205. DOI.
Ingleby, L.D., Spangler, S.R., Whiting, C.A.: 2007, Probing the large-scale plasma structure of the solar corona with Faraday rotation measurements. *Astrophys. J.* **668**, 520. DOI.
Kaltman, T.I., Bogod, V.M., Stupishin, A.G., Yasnov, L.V.: 2012, The altitude structure of the coronal magnetic field of AR 10933. *Astron. Rep.* **56**, 790. DOI.
Kim, R.-S., Gopalswamy, N., Moon, Y.-J., Cho, K.S., Yashiro, S.: 2012, Magnetic field strength in the upper solar corona using white-light shock structures surrounding coronal mass ejections. *Astrophys. J.* **746**, 118. DOI.
King, J.H., Papitashvili, N.E.: 2005, Solar wind spatial scales in and comparisons of hourly wind and ACE plasma and magnetic field data. *J. Geophys. Res.* **110**, A02104. DOI.
Kumari, A., Ramesh, R., Kathiravan, C., Wang, T.J.: 2017, Addendum to: strength of the solar coronal magnetic field—a comparison of independent estimates using contemporaneous radio and white-light observations. *Solar Phys.* **292**, 177. DOI.
Leblanc, Y., Dulk, G.A., Bougeret, J.-L.: 1998, Tracing the electron density from the corona to 1 AU. *Solar Phys.* **183**, 165. DOI.
Lin, H., Kuhn, J.R., Coulter, R.: 2004, Coronal magnetic field measurements. *Astrophys. J.* **613**, L177. DOI.
Lin, H., Penn, M.J., Tomczyk, S.: 2000, A new precise measurement of the coronal magnetic field strength. *Astrophys. J.* **541**, L83. DOI.
Lowder, C., Qiu, J., Leamon, R.: 2017, Coronal holes and open magnetic flux over cycles 23 and 24. *Solar Phys.* **292**, 18. DOI.
Mancuso, S., Garzelli, M.V.: 2013a, Coronal magnetic field strength from type II radio emission: complementarity with Faraday rotation measurements. *Astron. Astrophys.* **560**, L1. DOI.
Mancuso, S., Garzelli, M.V.: 2013b, Radial profile of the inner heliospheric magnetic field as deduced from Faraday rotation observations. *Astron. Astrophys.* **553**, A100. DOI.
Mancuso, S., Spangler, S.R.: 2000, Faraday rotation and models for the plasma structure of the solar corona. *Astrophys. J.* **539**, 480. DOI.
Mancuso, S., Raymond, J.C., Kohl, J., Ko, Y.-K., Uzzo, M., Wu, R.: 2003, Plasma properties above coronal active regions inferred from SOHO/UVCS and radio spectrograph observations. *Astron. Astrophys.* **400**, 347. DOI.
Mann, G., Aurass, H., Klassen, A., Estel, C., Thompson, B.J.: 1999, Coronal transient waves and coronal shock waves. In: *Plasma Dynamics and Diagnostics in the Solar Transition Region and Corona*, *Proc. 8 SOHO Workshop*, *ESA SP-446*, 477.
Musmann, G., Neubauer, F.M., Lammers, E.: 1977, Radial variation of the interplanetary magnetic field between 0.3 AU and 1.0 AU. *J. Geophys.* **42**, 591.
Ness, N.F., Wilcox, J.M.: 1964, Solar origin of the interplanetary magnetic field. *Phys. Rev. Lett.* **13**, 461. DOI.
Ness, N.F., Wilcox, J.M.: 1965, Sector structure of the quiet interplanetary magnetic field. *Science* **148**, 1592. DOI.
Ness, N.F., Wilcox, J.M.: 1966, Extension of the photospheric magnetic field into interplanetary space. *Astrophys. J.* **143**, 23. DOI.
Ord, S.M., Johnston, S., Sarkissian, J.: 2007, The magnetic field of the solar corona from pulsar observations. *Solar Phys.* **245**, 109. DOI.
Parker, E.N.: 1958, Dynamics of the interplanetary gas and magnetic field. *Astrophys. J.* **128**, 664. DOI.
Pätzold, M., Bird, M.K., Volland, H., Levy, G.S., Siedel, B.L., Stelzried, C.T.: 1987, The mean coronal magnetic field determined from HELIOS Faraday rotation measurements. *Solar Phys.* **109**, 91. DOI.
Plyusnina, L.A.: 1985, The relationship between the interplanetary magnetic field inhomogeneous structure and the distribution of large-scale magnetic fields in the photosphere (1969 – 1975). *Solar Phys.* **102**, 191. DOI.
Poomvises, W., Gopalswamy, N., Yashiro, S., Kwon, R.-Y., Olmedo, O.: 2012, Determination of the heliospheric radial magnetic field from the standoff distance of a CME-driven shock observed by the *STEREO* spacecraft. *Astrophys. J.* **758**, 118. DOI.
Raouafi, N.E., Riley, P., Gibson, S., Fineschi, S., Solanki, S.K.: 2016, Diagnostics of coronal magnetic fields through the Hanle effect in UV and IR lines. *Front. Astron. Space Sci.* **3**, 20. DOI.
Riley, P., Ben-Nun, M., Linker, J.A., Mikic, Z., Svalgaard, L., Harvey, J., Bertello, L., Hoeksema, T., Liu, Y., Ulrich, R.: 2014, A multi-observatory inter-comparison of line-of-sight synoptic solar magnetograms. *Solar Phys.* **289**, 769. DOI.
Saito, K.: 1977, A study of the background corona near solar minimum. *Solar Phys.* **55**, 121. DOI.
Sakurai, T., Spangler, S.R.: 1994, The study of coronal plasma structures and fluctuations with Faraday rotation measurements. *Astrophys. J.* **434**, 773. DOI.

Scherrer, P.H., Wilcox, J.M.: 1972, The mean photospheric magnetic field from solar magnetograms: comparisons with the interplanetary magnetic field. *Solar Phys.* **22**, 418. DOI.
Scherrer, P.H., Wilcox, J.M., Kotov, V.A., Severny, A.B., Howard, R.: 1977, The mean magnetic field of the Sun—method of observation and relation to the interplanetary magnetic field. *Solar Phys.* **52**, 3.
Schmidt, J.M., Cairns, I.H., Gopalswamy, N., Yashiro, S.: 2016, Coronal magnetic field profiles from shock-CME standoff distances. *J. Geophys. Res.* **121**, 9299. DOI.
Severny, A.B., Wilcox, J.M., Scherrer, P.H., Colburn, D.S.: 1970, Comparison of the mean photospheric magnetic field and the interplanetary magnetic filed. *Solar Phys.* **15**, 3. DOI.
Smith, E.J., Balogh, A.: 1995, Ulysses observations of the radial magnetic field. *Geophys. Res. Lett.* **22**, 3317. DOI.
Spangler, S.R.: 2005, The strength and structure of the coronal magnetic field. *Solar Phys.* **121**, 189. DOI.
Villante, U., Mariani, F., Cirone, R.: 1982, Helios 1 + Helios 2: a summary of IMF observations performed in the inner solar system during 1975 – 1981. *Nuovo Cimento C* **5**, 497. DOI.
Virtanen, I., Mursula, K.: 2016, Photospheric and coronal magnetic fields in six magnetographs. I. Consistent evolution of the bashful ballerina. *Astron. Astrophys.* **591**, A78. DOI.
Virtanen, I., Mursula, K.: 2017, Photospheric and coronal magnetic fields in six magnetographs. II. Harmonic scaling of field intensities. *Astron. Astrophys.* **604**, A7. DOI.
Vršnak, B., Magdalenić, J., Aurass, H., Mann, G.: 2002, Coronal and interplanetary magnetic fields inferred from band-splitting of type II bursts. In: *Solar Variability: From Core to Outer Frontiers*, *The 10th. European Sol. Phys. Meeting*, *ESA SP-506* **1**, 409.
Warmuth, A., Mann, G.: 2005, A model of the Alfvén speed in the solar corona. *Astron. Astrophys.* **435**, 1123. DOI.
Wiegelmann, T.: 2004, Optimization code with weighting function for the reconstruction of coronal magnetic fields. *Solar Phys.* **219**, 87. DOI.
Wiegelmann, T., Petrie, G.J.D., Riley, P.: 2017, Coronal magnetic field models. *Space Sci. Rev.* **210**, 249. DOI.
Wilcox, J.M.: 1968, The interplanetary magnetic field. Solar origin and terrestrial effects. *Space Sci. Rev.* **8**, 258. DOI.
Wilcox, J.M., Ness, N.F.: 1967, Solar source of the interplanetary sector structure. *Solar Phys.* **1**, 437. DOI.
Xiong, M., Davies, J.A., Feng, X., Owens, M.J.: 2013, Using coordinated observations in polarized white light and Faraday rotation to probe the spatial position and magnetic field of an interplanetary sheath. *Astrophys. J.* **777**, 32. DOI.
You, X.P., Coles, W.A., Hobbs, G.B., Manchester, R.N.: 2012, Measurement of the electron density and magnetic field of the solar wind using millisecond pulsars. *Mon. Not. Roy. Astron. Soc.* **422**, 1160. DOI.
Zharkov, S.I., Gavryuseva, E.V., Zharkova, V.V.: 2007, The latitudinal distribution of sunspot areas and magnetic fields and their correlation with the background solar magnetic field in the cycle 23. *Adv. Space Res.* **39**, 1753. DOI.